Research Square

Preprints are preliminary reports that have not undergone peer review.
They should not be considered conclusive, used to inform clinical practice,
or referenced by the media as validated information.

# Scale-dependent stress drop scaling of induced earthquakes driven by tensile-to-shear transition: Evidence from the Gonghe EGS field, China

**Cong Jiang**
Institute of Geophysics China Earthquake Administration
**Changsheng Jiang**
jiangcs@cea-igp.ac.cn

Institute of Geophysics China Earthquake Administration https://orcid.org/0000-0002-6812-1875

**Research Article**

**Keywords:**

**Posted Date:** November 18th, 2026

**DOI:** https://doi.org/10.21203/rs.3.rs-11505756/v1

**License:** This work is licensed under a Creative Commons Attribution 4.0 International License.
Read Full License

# Scale-dependent stress drop scaling of induced earthquakes driven by tensile-to-shear transition: Evidence from the Gonghe EGS field, China

Cong Jiang[1)], Changsheng Jiang[1), 2), 3) *]

1) Institute of Geophysics, China Earthquake Administration, Beijing 100081, China

2) Beijing Baijiatuan Earth Science National Observation and Research Station, Beijing 100095, China

3) Key Laboratory of Earthquake Source Physics, China Earthquake Administration

*Corresponding Author: Changsheng Jiang (jiangcs@cea-igp.ac.cn)

**Abstract**: Stress drop scaling governs the accuracy of ground motion prediction, yet the self-similarity assumption for induced earthquakes remains contested due to potential methodological biases. Leveraging a natural laboratory setting at the Gonghe Enhanced Geothermal Systems (EGS) field, we utilized a high-quality microseismic dataset to investigate source scaling. By applying empirical Green's function spectral ratios combined with bootstrap resampling, we rigorously quantified source parameter uncertainties and tested scaling robustness across distinct geological contexts, ranging from homogeneous basement to fault-developed zones. Results reveal a significant positive correlation between stress drop and seismic moment, confirming non-self-similar behavior that remains robust across varying geological settings and operational phases. A critical observation is that P-wave scaling exponents (~0.72) systematically exceed S-wave exponents (~0.57), while the corner frequency ratio ($f_c^P / f_c^S$) evolves from ~1.0 toward the theoretical shear limit with increasing magnitude. We propose a coupled tensile-to-shear transition and geometric evolution model: small-magnitude events manifest as low-stress-drop tensile fractures, evolving into high-stress-drop shear faults with a geometric transition from isotropic to planar morphologies where the rupture length outpaces width. This study establishes the control of rupture mechanism transition on scaling laws, providing a physical framework for improving seismic hazard assessment in EGS projects.

**Keywords**: Induced seismicity; Enhanced Geothermal Systems (EGS); Stress drop; Scaling law; Rupture mechanism

**Key policy highlights**

- Induced earthquakes in the Gonghe EGS field exhibit scale-dependent stress drop scaling, challenging the constant stress drop assumption commonly used in seismic hazard assessment.
- Current ground motion prediction equations may systematically underestimate the high-frequency radiation risk for moderate induced earthquakes.
- The transition from tensile to shear rupture mechanisms controls stress drop scaling, suggesting that fluid injection protocols directly modulate seismic risk potential.
- We recommend incorporating magnitude-dependent stress drop models into seismic hazard frameworks for enhanced geothermal systems to optimize risk mitigation strategies.

## 1. Introduction

Earthquake stress drop ($\Delta\sigma_0$), as a key source parameter describing the intensity of stress release during fault slip, directly controls the high-frequency components of seismic radiation energy and rupture efficiency, serving as a core indicator for understanding earthquake rupture physics (Brune 1970; Kanamori and Anderson 1975). Within the framework of

classical seismology, based on the assumption of scale invariance in the rupture process, stress drop is often hypothesized to be a constant independent of earthquake size, satisfying a "self-similar" scaling relationship. This assumption, rooted in the scale invariance of the rupture process, predicts a scaling law where the seismic moment ($M_0$) and corner frequency ($f_c$) satisfy $M_0 \propto f_c^{-3}$, leading to a constant stress drop (Aki 1980). The self-similarity model not only bridges microscopic friction and macroscopic rupture theoretically but is also supported by laboratory rock mechanics experiments indicating that frictional behavior itself can produce approximately self-similar spectral shapes when frictional dissipation dominates (Kilgore and Beeler 2025). Due to its simplicity, this model is widely used in constructing Ground Motion Prediction Equations (GMPEs) and seismic hazard assessments (Baltay et al. 2025). However, the applicability of the self-similarity assumption to induced seismicity is facing severe challenges. If induced earthquakes strictly follow self-similarity, existing empirical relationships based on tectonic earthquakes can be directly extrapolated to engineering sites. Conversely, if stress drops of induced earthquakes vary systematically with magnitude, it may indicate the dominant role of fluid-rock interaction processes such as pore pressure diffusion, effective stress changes, or frictional weakening (Jeong et al. 2024), simultaneously implying that the high-frequency vibration risk from larger magnitude events may be severely underestimated by current models. Notably, while some studies based on large-scale statistical analyses suggest that stress drops of hydraulic fracturing-induced earthquakes show no systematic difference from natural tectonic earthquakes, exhibiting scale-invariant characteristics (*e.g.*, Tomic et al. 2009; Zhang et al. 2024), increasing evidence indicates that stress drop behavior in fluid injection environments may be more complex, and simple self-similar assumptions may mask unique rupture physical processes under fluid action.

With the accumulation of seismic records induced by global hydraulic fracturing and Enhanced Geothermal System (EGS) industrial activities, numerous observations reveal that stress drop behavior of induced earthquakes often significantly deviates from the self-similarity assumption (*e.g.*, Goertz-Allmann et al. 2011; Yu et al. 2020). In shale gas development areas like the Montney in Canada and geothermal fields like The Geysers, stress drop exhibits systematic variations with magnitude, depth, or distance from the injection well (Ji et al. 2024), implying that its scaling behavior may be modulated by multiple factors including fluid injection processes, fault structural complexity, and confining pressure environment. Zhang and Yang (2025) further pointed out that external perturbations may break self-similarity by altering effective stress or frictional properties. This observation leads to a core scientific question: Does fluid injection merely "trigger" fault rupture following natural scaling laws, or does it fundamentally "alter" the rupture physical mechanism of faults through pore pressure diffusion or frictional weakening? It is noteworthy that recent research on repeating earthquakes has revealed another non-self-similar mechanism. Lengliné et al. (2023), through numerical simulations, indicated that effective normal stress changes caused by fluid pressure fluctuations can lead to non-self-similar scaling where rupture size remains constant while stress drop changes significantly, interpreting this as an indicator that the fault is at a critical state of frictional instability. However, whether this mechanism based on the "fixed asperity" assumption can explain extensive induced earthquake sequences accompanied by rupture propagation in EGS sites remains unclear. Precise examination of the stress drop scaling law is the "fingerprint" for distinguishing between these two physical scenarios and revealing the microscopic mechanisms of fluid-rock interaction.

Despite its significant scientific importance, accurate judgment of stress drop self-similarity currently faces immense methodological challenges. Recent studies warn that observed "non-self-similar" phenomena may partly stem from biases in source parameter estimation rather than true physical processes. On one hand, stress drop estimation itself is susceptible to biases from path attenuation, site response, spectral fitting strategies, and source model selection (Abercrombie et al. 2025b; Shearer et al. 2024). For instance, Cochran et al. (2024) found that different spectral fitting strategies (e.g., linear or logarithmic sampling, different source model assumptions) introduce significant uncertainties, while Calderoni and Abercrombie (2024) and Bindi et al. (2024b) pointed out that inappropriate attenuation

corrections or prior constraints (*e.g.*, fixed reference event parameters) can produce magnitude-dependent pseudo-scaling signals. On the other hand, for events with complex rupture processes (*e.g.*, multiple sub-events, strong directivity), stress drops estimated by different methods can differ by orders of magnitude and may even introduce magnitude-dependent pseudo-scaling signals (Neely et al. 2024; Lin et al. 2025). Knudson et al. (2025) also noted that the trend of increasing stress drop with depth observed in time-domain methods may be an artifact from insufficient correction for shallow attenuation. Therefore, when interpreting whether induced earthquake stress drops are self-similar, it is urgent to distinguish between true physical mechanisms and methodological biases based on high-quality datasets, which has become a frontier topic that must be overcome in this field.

The Gonghe Basin EGS project in Qinghai provides a natural laboratory under controllable experimental conditions to resolve the aforementioned controversy. The project's three injection wells (GH-01, GH-02, GH-03) constitute an ideal comparative experimental system at an engineering scale: the reservoir sections are vertically located in the granite basement at depths of 3500–3900 m with horizontal spacings of only 180~380 m, and similar hydraulic fracturing protocols and fluid injection parameters were implemented (Yin et al. 2024). However, high-precision microseismic monitoring reveals essential differences in their seismic responses: microseisms in the GH-01 well area are diffusely distributed in relatively intact granite, whereas seismic activity in the GH-02 and GH-03 well areas shows significant clustering along pre-existing fault systems (Yin et al. 2025). This configuration of "similar injection, different geology" enables the separation of fluid effects from tectonic effects. Based on preliminary analysis of 6,869 relocated microseismic events at this site (Jiang et al. 2026), the spatiotemporal evolution of stress drop has shown characteristics of dual regulation by geological background and fluid processes: in the GH-01 well area, a significant increase in stress drop with distance was observed after shut-in, and the high-stress-drop area is highly coupled with the pore pressure diffusion front; whereas in the GH-02/03 well areas, stress drop did not exhibit clear spatiotemporal variation patterns, indicating that the inherent heterogeneity of faults may dominate the stress release process. However, whether these observations imply universal laws of rupture scaling, and whether the observed non-self-similarity represents a true physical signal or stems from uncertainty in parameter estimation, are questions urgently requiring verification through a rigorous statistical framework.

This study aims to systematically examine the robustness and physical essence of stress drop non-self-similarity using the multi-well induced earthquake dataset from the Gonghe EGS site through a rigorous statistical framework and multi-physical joint constraints. We employ a method combining Bootstrap resampling technique and Orthogonal Distance Regression (ODR) to rigorously quantify the measurement uncertainties of corner frequency, seismic moment, and stress drop, focusing on solving three key scientific problems: (1) Examining the robustness of non-self-similarity under different geological and operational conditions, or whether it is merely a local product of specific tectonic environments, by comparing scaling exponents between homogeneous reservoirs (GH-01) and fault-developed areas (GH-02/03), between injection and shut-in periods, between near-well and far-field areas, and among different depth intervals; (2) Revealing quantitative laws of continuous rupture geometry evolution from three-dimensional tensile micro-cracks to two-dimensional shear faults through joint analysis of the magnitude dependence of the P-wave to S-wave corner frequency ratio and the wave-type difference in stress drop scaling rates, providing a unified physical interpretation for non-self-similarity; (3) Strictly excluding potential contamination of observed scaling laws by methodological biases through sensitivity tests under multiple source model assumptions, establishing the reliability of non-self-similarity as an intrinsic property of fluid injection-induced earthquakes. By answering these questions, this study expects to transcend simple phenomenological description, establish quantitative theoretical links between rupture geometry scale evolution and scaling law parameters, provide a transferable physical framework for reconciling global induced earthquake observation controversies, and lay a solid physical foundation for developing ground motion

prediction models considering source scale dependence and seismic hazard assessment strategies for EGS.

## 2. Data and Methods

### 2.1 Study Area and Data Used

This study is based on the Gonghe Basin Enhanced Geothermal System (EGS) project site in Qinghai, which is located on the northeastern margin of the Qinghai-Tibet Plateau and is China's first demonstration project targeting granitic hot dry rock. The bedrock in the study area is mainly Triassic granite with a high geothermal gradient, providing excellent reservoir conditions (Feng et al. 2018; Zhang et al. 2018). Three injection wells (GH-01, GH-02, and GH-03) were deployed at the site. The well spacing is relatively close (reservoir section spacing 180~380 m), but the reservoir geological backgrounds differ significantly: GH-01 is located in relatively intact granite, while GH-02 and GH-03 are adjacent to pre-existing fault systems (Yin et al. 2025). Imaging logging results also show that natural fractures in the 3600–3800 m depth range of the GH-01 well area are mainly NE-trending, low-to-medium-angle (~50°) tensile fractures; whereas natural fractures are more developed in the GH-02 and GH-03 well areas, mainly NW-trending, medium-to-high-angle (50~80°) compressive fractures (Chen et al. 2026). This difference in natural fracture development makes the GH-01 well area more suitable as a representative of homogeneous basement, while the GH-02/03 well areas represent typical characteristics of fault-developed zones. This natural control condition of "spatial proximity, distinct geology" provides an ideal experimental field for separating the influence of geological background and fluid injection on stress drop scaling laws.

The seismic waveform data used in this paper originate from the dense microseismic monitoring network deployed during 2020~2021. This network consists of short-period seismometers, geophones, and accelerometers capable of high-quality recording of microseismic signals (Figure 1a). The seismic source parameter calculations used in this paper follow the research results of Jiang et al. (2026). That dataset contains key parameters such as stress drop ($\Delta\sigma_0$), moment magnitude ($M_w$), corner frequency ($f_c$), and scalar seismic moment ($M_0$) for 1,728 induced earthquake events. It should be noted that the construction of this dataset employed the Empirical Green's Function (EGF) method. Given that moment magnitudes ($M_w$) were not yet determined during the initial location phase and the local magnitudes ($M_L$) in the catalog contained significant measurement errors, we did not employ the conventional magnitude difference criterion. Instead, we utilized a spectral amplitude ratio criterion to constrain the relative source size. Specifically, for potential EGF events satisfying waveform similarity (cross-correlation coefficient CC $\geq$ 0.6, Hartzell 1978), we calculated the median of the ratio of the three-component combined displacement spectra between the target earthquake and the EGF event in the 20~50 Hz frequency band; a median value greater than 10 was considered sufficient to ensure an adequate size difference between the events. Some microseismic events were not included because they could not be paired with EGF events satisfying the above conditions, so the final number of events with reliable source parameters (1,728) is lower than the total number of located earthquakes during that period. The magnitude range of these events covers $M_L$ -0.6 to 3.0, with focal depths mainly concentrated in the 3300~4400 m reservoir section (Figures 1b-d). Since the dataset calculation in Jiang et al. (2026) considered single "station-EGF event" pairs, whereas this study requires rigorous error assessment, the actual number of target earthquakes used for this study (with source parameter results) is lower than that in the dataset.

### 2.2 Methods for Earthquake Location and Source Parameter Calculation

Precise determination of source parameters is a prerequisite for examining stress drop self-similarity. The earthquake location and source parameter calculation workflow in this study follows the methodological system established by Jiang et al. (2026). Regarding earthquake location, Jiang et al. (2026) employed a joint inversion strategy combining VELEST absolute location and HypoDD double-difference relative location, using manually picked Pg and Sg phase data to obtain high-precision focal location results (Kissling et al.

1994; Waldhauser and Ellsworth 2000). This paper directly cites these relocation results as the geometric basis for source parameter analysis.

Regarding source parameter calculation, the Empirical Green's Function (EGF) spectral ratio method was used to calculate corner frequency ($f_c$), and scalar seismic moment ($M_0$) was calculated based on displacement spectral fitting. Particularly for the small-magnitude events focused on in this study, the EGF spectral ratio method has been proven to be the optimal method for microseismic measurement, effectively eliminating the influence of path attenuation and site effects and significantly reducing measurement errors compared to standard spectral fitting methods (Yu et al. 2020; Goertz-Allmann et al. 2011). For corner frequency $f_c$ determination, by calculating the spectral ratio between the target earthquake and the EGF event, common influences such as propagation path attenuation and site response are effectively eliminated, and nonlinear fitting is performed using the Boatwright (1980) model:

$$\Omega(f)=\frac{\Omega_0}{[1+(\frac{f}{f_c})^{\gamma n}]^{\frac{1}{\gamma}}}, \quad (1)$$

where $\Omega_0$ is the low-frequency plateau amplitude, $f_c$ is the corner frequency, $\gamma$=2, and $n$=2.

For scalar seismic moment $M_0$ calculation, Jiang et al. (2026) implemented a rigorous correction procedure to ensure the accuracy of absolute source parameters: first, the Horizontal-to-Vertical Spectral Ratio (HVSR) method was used to estimate and remove the site response function for each station, eliminating the amplification effect of shallow sedimentary layers on seismic wave amplitudes; second, a multi-station joint inversion determined the quality factor ($Q$) model for the study area, correcting for inelastic attenuation effects on seismic wave propagation paths. On the corrected displacement spectrum basis, scalar seismic moment $M_0$ was calculated by combining parameters such as hypocentral distance, wave velocity, and medium density (Hanks and Kanamori 1979), and then converted to moment magnitude $M_w$.

Stress drop $\Delta\sigma_0$ calculation is based on a circular rupture model (Eshelby 1957), with the calculation formula:

$$\Delta\sigma_0=\frac{7}{16}\frac{M_0}{r^3}*10^{-6}, \quad (2)$$

where rupture radius $r$ is derived from the corner frequency via the relation $r=k_c/f_c$ (Brune 1970). The model constant k refers to the study by Sato and Hirasawa (1973), taking 0.25 for P-waves and 0.32 for S-waves. This choice of parameters ensures consistency between P-wave and S-wave calculation results. It should be emphasized that the above standard procedure provides point estimates of source parameters, and the work of Jiang et al. (2026) focused on the spatiotemporal heterogeneity analysis of stress drop. However, when the research perspective shifts to examining the self-similarity of scaling laws, the potential influence of measurement errors in source parameter estimation (*e.g.*, non-uniqueness in EGF event selection, spectral ratio fitting residuals) on the scaling relationship shape cannot be ignored. Therefore, on this basis, this paper focuses on introducing Bootstrap resampling and Orthogonal Distance Regression (ODR) methods to strictly quantify and analyze these uncertainties, as detailed in Section 2.3.

### 2.3 Source Parameter Error Estimation and Orthogonal Regression Analysis

This study employs a method combining Bootstrap resampling technique and Orthogonal Distance Regression (ODR) to systematically estimate the measurement uncertainties of corner frequency, scalar seismic moment, and stress drop, and to examine the self-similarity of rupture scaling laws on this basis.

[1] **Error Estimation for Corner Frequency.** Corner frequency determination is based on the averaging of spectral ratio curves from multiple stations and multiple Empirical Green's Function (EGF) events. The traditional single-measurement standard deviation cannot capture uncertainties from the hierarchical data structure of "station-EGF event" pairs. This study uses Bootstrap resampling to estimate confidence intervals: the original dataset is treated as $K$ "station-EGF event" pairs, a virtual dataset is constructed by randomly sampling $K$ pairs with replacement, and the spectral ratio normalization, geometric mean stacking, and Boatwright model fitting procedures are re-executed to obtain a single corner frequency

estimate. This process is repeated $B$=1000 times to obtain an empirical distribution. The final corner frequency result is the geometric mean $f_c=10^{\frac{1}{B}\sum_{b=1}^{B}\log_{10} f_c^b}$, with the logarithmic standard deviation as the standard error. This method effectively quantifies the sensitivity of corner frequency estimation to different station combinations and EGF event selections. In the actual Bootstrap resampling estimation process, we set $K\geq 3$, under which condition source parameter calculation results were obtained for 719 target earthquakes in the P-wave group, 612 target earthquakes in the S-wave group, and 551 target earthquakes with both P-wave and S-wave calculation results. The magnitude range of these events covers $M_w$ 0.21~2.2.

[2] **Error Estimation for Scalar Seismic Moment.** The random error of scalar seismic moment originates from the dispersion in measuring the low-frequency level $\Omega_0$ at each station that recorded the target earthquake. For each target earthquake, each station independently calculates single-station scalar seismic moment $M_{0,i}$ according to formula (2), taking the logarithmic mean $\log_{10} M_0 = \frac{1}{N_{station}}\sum_{i=1}^{N_{station}} \log_{10} M_{0,i}$ as the final result, with the logarithmic standard deviation $\sigma_{\log_{10} M_0}$ as the relative error measure. Its 95% confidence interval is $[10^{\log_{10} M_0 - 1.96\sigma_{\log_{10} M_0}},\ 10^{\log_{10} M_0 + 1.96\sigma_{\log_{10} M_0}}]$.

[3] **Error Estimation for Stress Drop.** Stress drop is calculated from corner frequency and scalar seismic moment, and its error is estimated through error propagation theory. The variance of the logarithmic stress drop is: $\sigma^2_{\log_{10}\Delta\sigma_0}=\sigma^2_{\log_{10} M_0}+9\sigma^2_{\log_{10} f_c}$. The final stress drop result is calculated from the Bootstrap-estimated $f_c$ and the single-station averaged $M_0$, with its 95% confidence interval constructed according to the above logarithmic error propagation formula.

[4] **Error Estimation for the P-wave to S-wave Corner Frequency Ratio.** The P-wave to S-wave corner frequency ratio $f_c^P/f_c^S$ is used to constrain the geometric characteristics of the source rupture. This ratio is estimated through joint Bootstrap sampling: in each iteration, P-wave and S-wave data are resampled synchronously, and $f^b_{c,P}$ and $f^b_{c,S}$ are calculated separately to obtain a ratio sample $R(b)=f^b_{c,P}/f^b_{c,S}$. The final ratio result is the geometric mean $R=10^{\frac{1}{B}\sum_{b=1}^{B}\log_{10} R^b}$, with the logarithmic standard deviation as the error measure. This processing automatically includes the covariance information between $f^b_{c,P}$ and $f^b_{c,S}$.

[5] **Orthogonal Distance Regression and Self-similarity Test.** To examine the self-similarity of rupture scaling laws, this study employs ODR to fit the scaling relationships of $\log_{10} f_c$ *vs.* $\log_{10} M_0$ and $\log_{10}\Delta\sigma_0$ *vs.* $\log_{10} M_0$. Compared to traditional least squares regression, ODR simultaneously considers measurement errors in both independent and dependent variables, obtaining unbiased parameter estimates by minimizing orthogonal distance weighted residuals. For the $\log_{10} f_c$ vs. $\log_{10} M_0$ relationship, the theoretical self-similar model predicts a slope $a = -1/3$ (*i.e.*, $M_0 \propto f_c^{-3}$); for the $\log_{10}\Delta\sigma_0$ vs. $\log_{10} M_0$ relationship, the self-similar model predicts a slope $a = 0$ (stress drop is constant). This paper tests the significance of the difference between the observed slope and the theoretical value by constructing a $t$-statistic, where $t=(a_{obs}-a_{theory})/\sigma_a$, with $\sigma_a$ being the standard error of the slope output by ODR. Under the null hypothesis $H0$: $a=a_{\text{theory}}$ (*i.e.*, the data conform to the self-similar model), this statistic follows a $t$-distribution with degrees of freedom $v=n-2$ ($n$ is the sample size, and 2 is the number of linear model parameters). A two-tailed test is used to calculate the $p$-value: $p=2\times(1-F_t(|t|;v))$, where $F_t$ is the cumulative distribution function of the $t$-distribution. The 95% confidence interval (CI) for the slope is: $CI_{95\%} = a_{obs} \pm t_{0.975,\upsilon}\cdot\sigma_a$ is the 97.5th percentile of the $t$-distribution. This confidence interval has a duality with the hypothesis test: since the theoretical value $a_{\text{theory}}$ (-1/3 or 0) falls outside the 95% confidence interval, it further confirms that the observed scaling law significantly deviates from the self-similar model.

## 3. Results

### 3.1 General Characteristics and Statistical Significance of Stress Drop Scaling Laws

Using the source parameter error estimation results obtained in this study for 719 target earthquakes in the P-wave group, 612 in the S-wave group, and 551 target earthquakes with both P-wave and S-wave calculation results, we first examined the scaling relationship between stress drop ($\Delta\sigma_0$) and seismic moment ($M_0$) at the full-sample scale. The magnitude range of this dataset covers $M_w$ 0.21~2.2, with focal depths mainly concentrated in the 3300~4400 m reservoir section. The uncertainties in source parameters have been rigorously quantified through Bootstrap resampling, providing a solid sample foundation for statistical scaling laws.

Figure 2a and 2b show the scaling between corner frequency ($f_c$) and seismic moment ($M_0$) derived from P-wave and S-wave data, respectively, while Figures 2c and 2d show the scaling between stress drop ($\Delta\sigma_0$) and seismic moment ($M_0$) derived from P-wave and S-wave data, respectively. The Orthogonal Distance Regression (ODR) fitting results clearly show that for both P-waves and S-waves, stress drop exhibits a trend of significant increase with increasing seismic moment, presenting clear non-self-similar characteristics. For P-wave data, the scaling exponent (slope $a_P$) fitting result is 0.717 ± 0.011; for S-wave data, the scaling exponent (slope $a_S$) is 0.567 ± 0.014. Statistical tests indicate that the 95% confidence intervals for both do not contain the theoretical self-similar prediction value (slope = 0), and the $p$-values from the $t$-test are both far less than 0.001, thus strictly rejecting the null hypothesis of constant stress drop in statistics.

Furthermore, we note that the absolute value distribution range of stress drop is wide (0.01~2.0 MPa), exhibiting the high dispersion characteristic commonly seen in induced earthquake research. However, despite the dispersion, the overall trend of positive scaling is statistically extremely robust. This overall characteristic establishes the scale dependence of the rupture process of induced earthquakes in the Gonghe EGS site, meaning that larger magnitude earthquakes tend to release higher stress drops, which differs significantly from the self-similarity often reported for traditional intraplate tectonic earthquakes.

### 3.2 Robustness Test of Scaling Relationships

Do the observed non-self-similar scaling relationships stem from specific geological environments or engineering disturbances? To answer this question, we conducted grouped regression analyses by dividing the dataset according to geological background (GH-01 homogeneous basement *vs*. GH-02/03 fault-developed zones), operational phase (injection period *vs*. shut-in period), spatial location (near-well *vs*. far-field), and depth intervals.

First, the coupling effect between geological background and distance is noteworthy (Figures 3a-d). Although the GH-01 and GH-02/03 well areas differ significantly in reservoir heterogeneity, their stress drop scaling exponents both exhibit consistent non-self-similar characteristics (slope significantly greater than 0). However, the distance effect differs notably under different geological backgrounds. In the relatively homogeneous GH-01 well area (Figure 3a), the P-wave slopes for the near-well zone ($d \leq 200$ m) and far-field zone ($d > 200$ m) are 0.752 and 0.727, respectively, showing a weak difference, indicating that the scaling law is little affected by distance. In the fault-developed GH-02 well area (Figure 3b), the scaling exponent exhibits strong distance dependence: the P-wave slope (0.893) in the far-field zone ($d > 200$ m) is significantly higher than that in the near-well zone (0.666), and the S-wave slope shows the same trend. This phenomenon may be related to the development of numerous low-stress-drop tensile micro-ruptures in the near-well zone of the GH-02 area, whereas far-field events more likely activate high-stress-drop shear faults, leading to an increase in slope with distance. The GH-03 well area exhibits relatively good stability (Figure 3c).

Second, the influence of depth and operational phase is limited. In the depth-grouped analysis (Figure 3 e-h), the fitting results for the vast majority of intervals support the trend of increasing stress drop with seismic moment. It is worth noting that the S-wave fitting for the shallow interval (3300~3600 m) in the GH-02 well area showed a negative slope anomaly (-0.168 ± 0.313), but this result was supported by very few samples and accompanied by a large standard error; it is not statistically significant and did not alter the overall robustness of the scaling law (Figure 3f). In the injection phase grouping (Figure 3i-l), the combined

full-sample results (Figure 3l) show that the difference in scaling exponents between the injection and shut-in periods is extremely small (P-wave difference <0.01, S-wave difference <0.01), indicating that the time effect of fluid injection on the scaling law can be ignored.

Finally, a key phenomenon throughout is the systematic difference between P-wave and S-wave scaling exponents. In all grouped tests, the scaling exponent calculated from P-waves is consistently higher than that from S-waves. Combining the full-sample results, the P-wave slope (~0.72) is on average about 0.15 units higher than the S-wave slope (~0.57), and this difference is statistically significant. This "wave-type difference" suggests that there are intrinsic differences in the response mechanisms of P-wave and S-wave radiation spectra to changes in source geometry, providing a key entry point for subsequently constraining rupture geometry evolution through spectral characteristics.

### 3.3 Constraints of Corner Frequency Ratio on Rupture Geometry

To explore the physical roots behind non-self-similar scaling, particularly to explain the systematic difference between P-wave and S-wave scaling exponents, we analyzed the variation of the corner frequency ratio ($f_c^P/f_c^S$) with seismic moment $M_0$ (Figure 4a and 4b). This ratio is independent of the static stress drop calculation process and can directly reflect the pulse nature of the source time function, thereby constraining the rupture geometry. The analysis results show a significant positive correlation between $\log_{10}(f_c^P/f_c^S)$ and $\log_{10} M_0$, with fitted slopes of 0.049 (based on P-wave $M_0$, Figure 4a) and 0.074 (based on S-wave $M_0$, Figure 4b). This means that as earthquake scale increases, the ratio systematically increases.

Specifically, at the lower limit of the observed magnitude range ($M_0$=$10^9$~$10^{10}$ N·m), the ratio is mainly distributed in the range of 0.8~1.2, significantly deviating from the theoretical prediction of the classical shear rupture model (1.44~1.60), but highly consistent with predictions from tensile rupture models containing significant isotropic components. This indicates that small-magnitude events may be dominated by fluid pressure, undergoing three-dimensional tensile rupture with volumetric expansion characteristics. In the larger magnitude range ($M_0$>$10^{11}$ N·m), the ratio shows a trend approaching the theoretical value for shear rupture, with the ratio center rising to the 1.1~2.0 interval, indicating an evolution of rupture mechanism toward pure shear dislocation.

This observational result quantitatively characterizes the evolutionary path of rupture geometry. Based on the evolutionary trend of the corner frequency ratio, we can delineate different physical domains of rupture evolution through scalar seismic moment ($M_0$) (Figure 5): When $M_0$<$10^{10}$ N·m, the ratio is close to 1.0, indicating that small-magnitude events tend to exhibit approximately isotropic three-dimensional rupture characteristics ($L \approx W$); when $M_0$>$10^{11.5}$, the ratio shows a trend approaching the theoretical shear rupture value (~1.44), indicating that large-magnitude events have transitioned to asymmetric planar shear ruptures ($L >> W$). The transitional domain between the two reflects the continuous evolution of rupture geometry. This geometric evolution model can not only explain the magnitude dependence of the ratio but also provides a unified physical explanation for the phenomenon where the P-wave stress drop scaling exponent is significantly higher than the S-wave exponent—*i.e.*, the P-wave spectrum is more sensitive to the rupture's short axis (width $W$), while the S-wave spectrum is primarily controlled by the rupture's long axis (length $L$), and the differential evolution of the aspect ratio leads to a separation in wave-type scaling exponents.

## 4. Discussion

### 4.1 Observational Reliability of Non-self-similarity: Error Quantification and Bias Exclusion

The uncertainty in stress drop estimation has been widely confirmed in seismology research; results from different analytical methods for the same earthquake sequence can differ by orders of magnitude, mainly stemming from subjectivity in source spectral fitting strategies, uncertainty in path attenuation corrections, and complexity of the source time function (Cochran et al., 2024; Neely et al. 2024; Abercrombie et al. 2025a). However, the

non-self-similar scaling relationship observed in this study does not arise from artifacts of the aforementioned methodological biases but reflects the physical essence of the earthquake rupture process within the Gonghe EGS site. We excluded the possibility that the observational results are dominated by methodological noise through evidence from three levels.

First, the use of the Empirical Green's Function (EGF) method effectively suppresses interference from non-source factors. The community validation study by Cochran et al. (2024) indicates that the choice of spectral fitting method can lead to significant differences in stress drop estimates. Compared to standard spectral fitting methods, the EGF spectral ratio technique used in this study fundamentally avoids systematic biases introduced by inaccurate attenuation models or site effect corrections by eliminating the common influence of propagation path attenuation and site response (Calderoni and Abercrombie 2024). Particularly for the small-magnitude events focused on in this study, the EGF spectral ratio method has been proven to be the optimal method for microseismic measurement, effectively eliminating the influence of path attenuation and site effects and significantly reducing measurement errors compared to standard spectral fitting methods (Yu et al. 2020; Goertz-Allmann et al. 2011). Chang et al. (2023) pointed out that lateral variations in site effects can lead to about 13% dispersion in stress drop, and this property of the EGF method ensures that the observed scaling trend is not contaminated by path or site effects.

Second, the consistency between P-wave and S-wave results provides independent cross-validation. Bindi et al. (2024a) noted that inappropriate reference event constraints may introduce pseudo-scaling signals. In this study, P-wave and S-wave data were processed through independent workflows, yet both exhibited significant and consistent positive scaling relationships (slopes of approximately 0.70 and 0.55, respectively). If the observed trend were purely methodological error or random noise, it would be difficult to explain why both wave types synchronously deviate from the self-similarity assumption (slope = 0) and exhibit a systematic difference (P-wave slope > S-wave slope). This intrinsic consistency between wave types strongly proves that the observed signal originates from the source itself.

Finally, robustness across geological and engineering conditions excludes the influence of local interference factors. Research by Neely et al. (2024) and Lin et al. (2025) indicates that source complexity (*e.g.*, directivity, non-circular rupture) can lead to large scatter in stress drop estimates. However, this study observed highly consistent scaling exponents across different hydraulic fracturing wells (homogeneous basement GH-01 and fault-developed zones GH-02/03), different operational phases (injection and shut-in periods), and different spatial locations (near-well vs. far-field, different depths). This consistency across significant geological differences and fluid pressure states indicates that non-self-similarity is not a local product of specific tectonic environments, nor can it be random source complexity noise—the latter should manifest as discrete bias patterns in different subsets rather than a robust linear trend. Therefore, although inherent uncertainties remain in stress drop estimates for individual events, the statistically robust trend confirms the objective existence of the non-self-similar scaling relationship.

### 4.2 Rupture Geometric Evolution Mechanism: From Three-dimensional Tensile Fracture to Two-dimensional Shear Slip

The observational results show that the stress drop of Gonghe EGS induced earthquakes exhibits a significant positive scaling relationship with increasing seismic moment. To reasonably explain this phenomenon, relying solely on changes in rupture geometric scale is insufficient to describe the complete physical picture. We propose a "coupled tensile-to-shear transition and geometric evolution" model (Figure 5), arguing that the scale dependence of stress drop is essentially the macroscopic manifestation of the transition of rupture mechanism from fluid-dominated tensile fracture to tectonic-stress-dominated shear rupture, superimposed on the evolution of rupture geometry.

First, we discuss the controlling effect of the fluid pressure environment on the absolute value of stress drop. The study by Lengliné et al. (2023) shows that in fluid-pressure-active regions, a reduction in effective normal stress leads to significantly lower earthquake stress

drop, and rupture size exhibits approximately constant non-self-similar characteristics. In this study, the extremely low stress drop levels for small-magnitude events (some below 0.1 MPa) are attributed not only to the tensile rupture mechanism but also to their occurrence in near-well zones with high pore pressure and low effective stress, which aligns with the physical understanding that "low effective stress leads to low stress drop". However, unlike the "fixed-size" repeating earthquakes simulated by Lengliné et al. (2023), we observed a weak growth trend of rupture radius $r$ with seismic moment $M_0$ ($r \propto M_0^{0.1}$), indicating that EGS induced earthquakes are not simple repeated ruptures but are accompanied by rupture scale expansion. Therefore, the positive scaling of stress drop is the result of a dual mechanism superposition.

The core of this model lies in the "mechanism transition" controlling the overall level of stress drop. In the microseismic stage (Figure 5a), high pore pressure generated by fluid injection causes tensile fracture in the rock. At this time, the low effective stress environment inhibits fault strength; theoretically, the static stress drop of a purely tensile fracture is significantly lower than that of a shear fracture of the same scale. At this stage, ruptures present as disordered three-dimensional clusters, geometrically approximately isotropic ($L \approx W$), and the overall level of stress release is low, thus pulling down the average stress drop level for small-magnitude events. This observation is supported by experimental rock physics research: Naoi et al. (2020) found in laboratory hydraulic fracturing experiments that stress drops for tensile-dominant fracture events are significantly lower than for shear-type fractures; Martínez-Garzón et al. (2017), in their study of induced earthquakes in geothermal fields, also confirmed that events with significant non-double-couple components (indicating tensile components) have generally lower stress drops than pure shear double-couple events. This provides a direct physical mechanism explanation for the observed low-stress-drop characteristic at small magnitudes. However, as seismic moment increases, the rupture enters a transitional stage (Figure 5b), where fluid pressure effects weaken, effective normal stress recovers, and tectonic stress begins to dominate the rupture process, manifesting as a tensile-shear hybrid mode. Because shear rupture has higher stress release efficiency, stress drop increases systematically with magnitude, eventually evolving into a mature high-stress-drop shear fault (Figure 5c).

Notably, the difference between P-wave and S-wave scaling exponents ($a_P > a_S$) provides a key geometric constraint for the above model, revealing the geometric evolution process accompanying the mechanism transition. According to the geometric relationship shown in Figure 5, as rupture scale expands, the geometry evolves from three-dimensional clusters to two-dimensional planar faults ($L >> W$). In this process, the S-wave corner frequency is mainly controlled by the rupture's long axis ($L$), while the P-wave corner frequency is more sensitive to the short axis ($W$). Because the long axis $L$ expands rapidly along the fault strike, its growth rate is significantly faster than that of the short axis $W$, leading to a relatively smaller (slower-growing) source scale $r_P$ inverted from P-waves. According to the stress drop formula $\Delta\sigma_0 \propto M_0/r^3$, a smaller scale growth rate means that P-wave stress drop increases more with magnitude than S-wave stress drop, resulting in a systematically higher P-wave scaling exponent than S-wave. This theoretical deduction is highly consistent with the observed trend of the ratio $f_c^P / f_c^S$ evolving from 1.0 to 1.44, confirming the continuous evolution of rupture geometry from isotropic to planar morphology.

Independent observational evidence further supports the plausibility of this model. Zhou et al. (2025), using moment tensor inversion for microseismic events at the Gonghe EGS site, found that while double-couple (DC) components dominate, significant non-double-couple components still exist, indicating that the rupture process contains tensile components. The theoretical study by Vavryčuk (2011) points out that with increasing seismic moment, the slope parameter $S_a$ gradually decreases, and the ISO component gradually converts to a DC component, which aligns with the trend observed in this study of stress drop systematically increasing with magnitude. In summary, the non-self-similar scaling revealed by this study is an extension of the existing theoretical framework: it encompasses both the modulating effect

of fluid pressure on effective stress (the absolute level of stress drop) and highlights the dominant role of rupture mechanism transition and geometric evolution (the growth trend of stress drop with magnitude).

### 4.3 Implications for the Universality of Induced Earthquake Source Physics

The rupture mechanism evolution law revealed by this study is not unique to the Gonghe site but provides a universal framework for understanding the source physics of global fluid-induced earthquakes.

On one hand, the independence from geological background implies the controlling role of the fluid injection process itself. A striking observational fact is that despite significant differences in geological conditions (*e.g.*, fault development degree, lithological uniformity) among the GH-01, GH-02, and GH-03 well areas, their stress drop scaling exponents exhibit high consistency. Unlike tectonic earthquakes often controlled by the geometry of pre-existing faults, the initiation and propagation of induced earthquakes are more jointly controlled by fluid pressure diffusion pathways and the rock's primary fracture network. Studies by Fischer and Guest (2011) and Šílený et al. (2009) both point out that fluid injection tends to preferentially activate disordered micro-cracks, producing tensile fractures with positive volumetric expansion. The consistency across geological differences found in this study indicates that the fluid injection process itself may be the primary factor reshaping rupture geometry and driving evolution from disordered three-dimensional tensile fractures to ordered two-dimensional shear fractures. This finding reconciles controversies over induced earthquake scaling laws in different geological settings.

On the other hand, this model provides a physical explanation for understanding the difference in stress drop magnitude between induced and tectonic earthquakes. Jeong and Lui (2024), in their study of the St. Gallen geothermal project in Switzerland, found that stress drops for induced earthquakes are significantly lower than for tectonic earthquakes. Based on the model in this study, this can be attributed to the inclusion of numerous fluid-driven low-stress-drop tensile micro-ruptures in induced earthquake sequences, thus lowering the overall stress drop level. As magnitude increases, rupture transitions to a high-stress-drop shear mechanism, and stress drop increases with magnitude, explaining why induced earthquakes often exhibit non-self-similar characteristics, whereas large-magnitude tectonic earthquakes (mostly mature shear ruptures) are closer to self-similarity.

Finally, the findings of this study have direct implications for seismic risk assessment in EGS engineering practice. Traditional Ground Motion Prediction Equations (GMPEs) typically assume constant stress drop (*i.e.*, the self-similarity assumption), which may lead to systematic underestimation of ground motion parameters for moderate-strength induced earthquakes. According to the results of this study, as magnitude increases, the rupture mechanism transitions to shear dominance and the geometry becomes more planar, and its high-frequency radiation capability may be stronger than predictions based on the constant stress drop assumption. Therefore, in hazard assessment for EGS induced earthquakes, magnitude-dependent stress drop models should be introduced to more accurately predict potential maximum ground motion, thereby optimizing hydraulic fracturing operational parameters and developing more rational risk control strategies.

## 5. Conclusions

Addressing the core controversy over whether stress drops of fluid injection-induced earthquakes follow self-similar scaling laws, this paper, based on high-precision microseismic events recorded from three hydraulic fracturing wells at the Qinghai Gonghe EGS project, rigorously quantified source parameter uncertainties using Bootstrap resampling and Orthogonal Distance Regression, and systematically examined the robustness of stress drop scaling laws across different geological backgrounds, operational phases, and spatial locations. The main conclusions are as follows:

(1) Stress drop exhibits a significant non-self-similar scaling relationship with seismic moment. The full-sample P-wave scaling exponent is approximately 0.72, and the S-wave exponent is approximately 0.57, both significantly deviating from the self-similarity

assumption. This characteristic has overall robustness across geological backgrounds and operational phases, but shows clear distance dependence in the fault-developed zone (GH-02), where the slope in the near-well zone is significantly lower than in the far-field zone, revealing the modulating effect of fluid pressure distribution on local scaling laws.

(2) A "coupled tensile-to-shear transition and geometric evolution" model is proposed. The systematically higher P-wave scaling exponent than S-wave (difference ~0.15) is a core finding of this study. Combined with the trend of the corner frequency ratio ($f_c^P / f_c^S$) evolving from approximately 1.0 toward the theoretical shear rupture prediction value (1.44) with increasing seismic moment, this reveals dual evolutionary laws of rupture physical mechanism with magnitude: on one hand, the rupture mechanism transitions from fluid-driven low-stress-drop tensile fracture to tectonic high-stress-drop shear rupture, controlling the overall increase in stress drop level; on the other hand, the rupture geometry evolves from three-dimensional isotropy ($L \approx W$) to two-dimensional planar ($L >> W$), causing the P-wave stress drop, which is more sensitive to the short axis, to increase faster than the S-wave stress drop. This model successfully reconciles the observational contradiction where the ratio is ~1.0 at small magnitudes and approaches the classical shear limit at large magnitudes, and distinguishes the essential difference in the causes of scaling laws between EGS induced earthquakes and typical repeating earthquakes.

(3) The physical framework established in this study provides key constraints for improving induced earthquake ground motion prediction models. The results indicate that traditional Ground Motion Prediction Equations (GMPEs) based on the constant stress drop assumption may systematically underestimate the high-frequency radiation capability of moderate-strength induced earthquakes. It is recommended that magnitude-dependent stress drop scaling models be introduced in future EGS seismic hazard assessments to more accurately predict potential ground motion parameters and optimize risk control strategies. Meanwhile, the mechanism evolution laws revealed by this study are universal, providing a unified physical perspective for explaining differences in stress drop scaling across different injection sites globally.

## CREDIT AUTHORSHIP CONTRIBUTION STATEMENT

**Cong Jiang**: Data curation, Formal analysis, Writing – original draft, Methodology, Visualization. **Changsheng Jiang**: Conceptualization, Methodology, Funding acquisition, Project administration, Supervision, Writing – review & editing.

## CONFLICT OF INTEREST

The authors declare that there is no conflict of interest regarding the publication of this manuscript.

## ACKNOWLEDGMENTS

This study was jointly supported by the Independent Research Projects of the Institute of Geophysics, China Earthquake Administration (Grant Nos. JY2022Z13 and JY2023Z05). We thank Dr. Yan Zhang, Dr. Xiaolin Hou, Master's student Jiashan Zhang, and Ph.D. candidate Zan Li from the Institute of Geophysics, China Earthquake Administration for their valuable suggestions. We also acknowledge the Center for Hydrogeology and Environmental Geology Survey, China Geological Survey for providing the seismic waveform data.

## DATA AVAILABILITY

The seismic waveform data used in this study were provided by the Center for Hydrogeology and Environmental Geology Survey, China Geological Survey. Due to data policy restrictions, these data are not publicly available. All other data supporting the findings of this study are available from the published sources listed in the references.

## REFERENCES

621 Abercrombie RE, et al. 2025. Overview of the SCEC/USGS community stress drop validation
622 study using the 2019 Ridgecrest earthquake sequence. Bull Seismol Soc Am.
623 115(3):734-759. https://doi.org/10.1785/0120240158
624 Abercrombie RE, Chen X, Huang Y, Chu S. 2025. Comparison of EGF methods for Ridgecrest
625 sequence: can EGFs help resolve ambiguity in isolating source spectra? Bull Seismol Soc
626 Am. 115:1132-1148. https://doi.org/10.1785/0120240161
627 Aki K. 1980. Quantitative seismology. Theory and Method. 304-308.
628 Baltay A, Abercrombie RE, Oth A, Uchide T. 2025. Introduction to the special section on
629 improving measurements of earthquake source parameters. Bull Seismol Soc Am.
630 115:723-733. https://doi.org/10.1785/0120250055
631 Bindi D, et al. 2024. Numerical tests to evaluate the effect of constraining the spectral shape of
632 reference events on source parameter scaling. Bull Seismol Soc Am. 115(3):1062-1071.
633 https://doi.org/10.1785/0120240132
634 Bindi D, Spallarossa D, Picozzi M, Tarchini G. 2024. Scaling and depth variability of source
635 parameters in central and southern Italy using regional attenuation models. Bull Seismol
636 Soc Am. 115:983-999. https://doi.org/10.1785/0120240144
637 Boatwright J. 1980. A spectral theory for circular seismic sources; simple estimates of source
638 dimension, dynamic stress drop, and radiated seismic energy. Bull Seismol Soc Am.
639 70(1):1-27.
640 Brune JN. 1970. Tectonic stress and the spectra of seismic shear waves from earthquakes. J
641 Geophys Res Solid Earth. 75(26):4997-5009.
642 Calderoni G, Abercrombie RE. 2024. Combining two distinct methods to resolve spatial variation
643 in attenuation and earthquake source parameters. Bull Seismol Soc Am. 115:875-889.
644 https://doi.org/10.1785/0120240160
645 Chang H, et al. 2023. Quantifying site effects and their influence on earthquake source parameter
646 estimations using a dense array in Oklahoma. J Geophys Res Solid Earth.
647 128(9):e2023JB027144. https://doi.org/10.1029/2023JB027144
648 Chen D, et al. 2026. The fracture characteristics and dynamic response to hydraulic fracturing in
649 the Gonghe enhanced geothermal system (EGS) field, Qinghai Province, Northwest China.
650 Geothermics. 137:103623. https://doi.org/10.1016/j.geothermics.2026.103623
651 Cochran ES, et al. 2024. SCEC/USGS community stress-drop validation study: How spectral
652 fitting approaches influence measured source parameters. Bull Seismol Soc Am.
653 115:760-776. https://doi.org/10.1785/0120240140
654 Eshelby JD. 1957. The determination of the elastic field of an ellipsoidal inclusion, and related
655 problems. Proc R Soc Lond A. 241(1226):376-396.
656 Feng Y, et al. 2018. The geothermal formation mechanism in the Gonghe Basin. China Geol.
657 1:331-345.
658 Fischer T, Guest A. 2011. Shear and tensile earthquakes caused by fluid injection. Geophys Res
659 Lett. 38:L05307. https://doi.org/10.1029/2010GL045447
660 Goertz-Allmann BP, Goertz A, Wiemer S. 2011. Stress drop variations of induced earthquakes at
661 the Basel geothermal site. Geophys Res Lett. 38(9):L09308.
662 Hanks TC, Kanamori H. 1979. A moment magnitude scale. J Geophys Res Solid Earth.
663 84(B5):2348-2350.
664 Hartzell SH. 1978. Earthquake aftershocks as Green's functions. Geophys Res Lett. 5(1):1-4.

Jeong S, Lui SKY. 2024. Source characteristics of tectonic and induced events near St. Gallen, Switzerland: utilizing the empirical Green's function method and generalized inversion technique. Bull Seismol Soc Am. 115:1000-1015. https://doi.org/10.1785/0120240145

Jeong S, Tan X, Lui SKY. 2024. Fluid-induced aseismic slip may explain the non-self-similar source scaling of the induced earthquake sequence near the Dallas-Fort Worth Airport, Texas. J Geophys Res Solid Earth. 129:e2023JB027714. https://doi.org/10.1029/2023JB027714

Ji C, Archuleta RJ, Peyton A. 2024. Capturing broadband spectral characteristics of moderate-size earthquakes using nearby recordings: a case study of 42 *M*w 4.0–5.4 Ridgecrest earthquakes. Bull Seismol Soc Am. 115:850-874. https://doi.org/10.1785/0120240180

Jiang C, et al. 2026. Spatiotemporal heterogeneity of hydraulic fracturing-induced earthquake stress drops controlled by geological setting and fluid operations: Evidence from multi-well observations at the Gonghe EGS, China. Geophys J Int. (Submitted).

Kanamori H, Anderson DL. 1975. Theoretical basis of some empirical relations in seismology. Bull Seismol Soc Am. 65(5):1073-1095.

Kilgore B, Beeler NM. 2025. Earthquake stress drop, source spectra from laboratory experiments, and the apparent unsteadiness of frictional slip. Bull Seismol Soc Am. 115:1105-1131. https://doi.org/10.1785/0120240123

Kissling E, Ellsworth W, Eberhart-Phillips D, Kradolfer U. 1994. Initial reference models in local earthquake tomography. J Geophys Res Solid Earth. 99(B10):19635-19646.

Knudson TC, Ellsworth WL, Beroza GC. 2025. Source parameter analysis using maximum amplitudes in the time domain. Bull Seismol Soc Am. 115:839-849. https://doi.org/10.1785/0120240198

Lengliné O, Ampuero JP, Schmittbuhl J. 2023. Scaling of repeating earthquakes at the transition from aseismic to seismic slip. Geophys Res Lett. 50:e2022GL101604. https://doi.org/10.1029/2022GL101604

Lin YY, Schaal N, Lapusta N. 2025. On seismological stress-drop estimates for earthquake sources simulated on rate-and-state faults. Bull Seismol Soc Am. 115(3):1072-1104. doi:10.1785/0120240147

Martínez-Garzón P, Kwiatek G, Bohnhoff M, Dresen G. 2017. Volumetric components in the earthquake source related to fluid injection and stress state. Geophys Res Lett. 44:800-809.

Naoi M, et al. 2020. Tensile-dominant fractures observed in hydraulic fracturing laboratory experiment using Eagle Ford shale. Geophys J Int. 222(2):769-780. https://doi.org/10.1093/gji/ggaa183

Neely JS, Park S, Baltay A. 2024. The impact of source time function complexity on stress-drop estimates. Bull Seismol Soc Am. 115:1149-1161. https://doi.org/10.1785/0120240022

Sato T, Hirasawa T. 1973. Body wave spectra from propagating shear cracks. J Phys Earth. 21(4):415-431.

Shearer PM, et al. 2024. Earthquake source spectra estimates vary widely for two Ridgecrest aftershocks because of differences in attenuation corrections. Bull Seismol Soc Am. 115:777-791. https://doi.org/10.1785/012024013

Šílený J, Hill DP, Eisner L, Cornet FH. 2009. Non-double-couple mechanisms of microearthquakes induced by hydraulic fracturing. J Geophys Res Solid Earth. 114:B08307. doi:10.1029/2008JB005987

Tomic J, Abercrombie RE, do Nascimento AF. 2009. Source parameters and rupture velocity of small M < 2.1 reservoir induced earthquakes. Geophys J Int. 179(2):1013-1023.

Vavryčuk V. 2011. Tensile earthquakes: Theory, modeling, and inversion. J Geophys Res Solid Earth. 116:B12320. https://doi.org/10.1029/2011JB008770

Waldhauser F, Ellsworth WA. 2000. Double-Difference earthquake location algorithm: Method and application to the northern Hayward fault, California. Bull Seismol Soc Am. 90(6):1353-1368. https://doi.org/10.1785/0120000006

Yin XX, et al. 2024. Assessment and optimization of maximum magnitude forecasting models for induced seismicity in enhanced geothermal systems: The Gonghe EGS project in Qinghai, China. Tectonophysics. 886:230438. https://doi.org/10.1016/j.tecto.2024.230438

Yin XX, et al. 2025. Seismic activity reveals the coexistence of multiple mechanisms of fault reactivation induced by hydraulic fracturing in the Gonghe EGS Project in Qinghai, China. Seismol Res Lett. 96(3):1573-1589. https://doi.org/10.1785/0220240244

Yu H, et al. 2020. Well proximity governing stress drop variation and seismic attenuation associated with hydraulic fracturing induced earthquakes. J Geophys Res Solid Earth. 125(9):e2020JB020103.

Zhang C, et al. 2018. Terrestrial heat flow and crustal thermal structure of the Gonghe–Guide area, northeastern Qinghai–Tibetan Plateau. Geothermics. 72:182-192. https://doi.org/10.1016/j.geothermics.2017.11.011

Zhang JW, Yang HF, Zi JP, Su JR, Chen XW. 2024. An improved estimation of stress drop and its application on induced earthquakes in the Weiyuan Shale Gas Field in China. Geophys J Int. 236(3):1785-1803. https://doi.org/10.1093/gji/ggae014

Zhang J, Yang H. 2025. Improved source parameter estimation of earthquakes in the 2019 Ridgecrest sequence based on a global optimization algorithm and their implications on fault behaviors. Bull Seismol Soc Am. 115:805-824. https://doi.org/10.1785/0120240111

Zhou W, et al. 2025. Microseismic source mechanism inversion and interpretation for the injection test of hot dry rock in the Gonghe Basin. Chin J Geophys. 68(9):3464-3476. https://doi.org/10.6038/cjg2024S0327

## Figure captions

**Figure 1. Map of the study area, seismic network, and spatial distribution of earthquakes**. (a) Shows the distribution of seismic stations and well locations in the study area. The main map marks the wellheads of the three injection wells (GH-01, GH-02, GH-03) and the distribution of seismic stations; the inset in the upper right shows the location of the Gonghe site within China; the right panel shows the surface projection of well trajectories and the East-West depth profile. (b~d) Three-dimensional spatial distribution of earthquakes around wells GH-01, GH-02, and GH-03, respectively (depth range 3000~4500 m). In the figures, red dots represent events with stress drop results during the hydraulic fracturing period, orange diamonds represent events with stress drop results during the shut-in period, and gray dots represent events without stress drop results. The trajectory of the corresponding well is displayed in color, while the trajectories of the other two wells are shown in gray.

**Figure 2. Scaling relationships of corner frequency ($f_c$) and stress drop ($\Delta\sigma_0$) with seismic moment ($M_0$)**. (a) and (b) show the scaling between corner frequency ($f_c$) and seismic moment ($M_0$) derived from P-wave and S-wave data, respectively. (c) and (d) show the scaling between stress drop ($\Delta\sigma_0$) and seismic moment ($M_0$) derived from P-wave and S-wave data, respectively. Error bars are shown for each measurement. The solid red line represents the Orthogonal Distance Regression (ODR) fit, and the shaded pink area indicates the 95% confidence interval.

**Figure 3. Comprehensive comparison of stress drop scaling exponents across different geological backgrounds and multi-dimensional conditions**. The first three columns correspond to the GH-01, GH-02, and GH-03 well areas, respectively, while the fourth column represents the combined dataset. Rows represent different grouping conditions: (a~d) comparison between near-well (≤ 200 m) and far-field (> 200 m) zones; (e~h) comparison across depth intervals (overlying layer, stimulation interval, and underlying layer); (i~l) comparison between injection and shut-in phases. In all subplots, blue and red bars represent the scaling exponents for P-waves and S-waves, respectively, with error bars indicating the standard deviation of the fit.

**Figure 4. Variation of P-to-S corner frequency ratio ($f_c^P/f_c^S$) with seismic moment**. (a) and (b) show the ratio plotted against seismic moment estimated from P-wave and S-wave spectra, respectively. Error bars, the Orthogonal Distance Regression (ODR) fit line (solid red line), and the 95% confidence interval (shaded pink area) are shown.

**Figure 5. Conceptual model of rupture geometry and mechanism evolution with increasing scalar seismic moment ($M_0$)**. Based on the observed trend of the corner frequency ratio ($f_c^P/f_c^S$), the rupture process is divided into three physical domains. The y-axis represents stress drop, and the x-axis is scalar seismic moment $M_0$. (a) Tensile-dominant domain ($M_0<10^{10}$ N·m): Characterized by fluid-driven disordered micro-cracks. Ruptures are approximately isotropic ($L\approx W$), with $f_c^P/f_c^S$ ratios approaching 1.0 and low stress drops. (b) Transitional domain ($10^{10}< M_0 <10^{11.5}$ N·m): A hybrid tensile-shear mode. As rupture expands, shear components increase, and geometry evolves to be elliptical (length $L$ grows faster than width $W$). The $f_c^P/f_c^S$ ratio falls between 1.0 and the theoretical shear value, causing P-wave stress drop to increase faster than S-wave stress drop. (c) Shear-dominant domain ($M_0>10^{11.5}$ N·m): A mature 2D shear fault. The rupture forms a typical shear dislocation model with $L \gg W$. The $f_c^P/f_c^S$ ratio approaches the theoretical shear value (~1.44), and stress drop stabilizes at a higher level. The blue arrow indicates the overall increasing trend of stress drop driven by mechanism transition and geometric evolution.

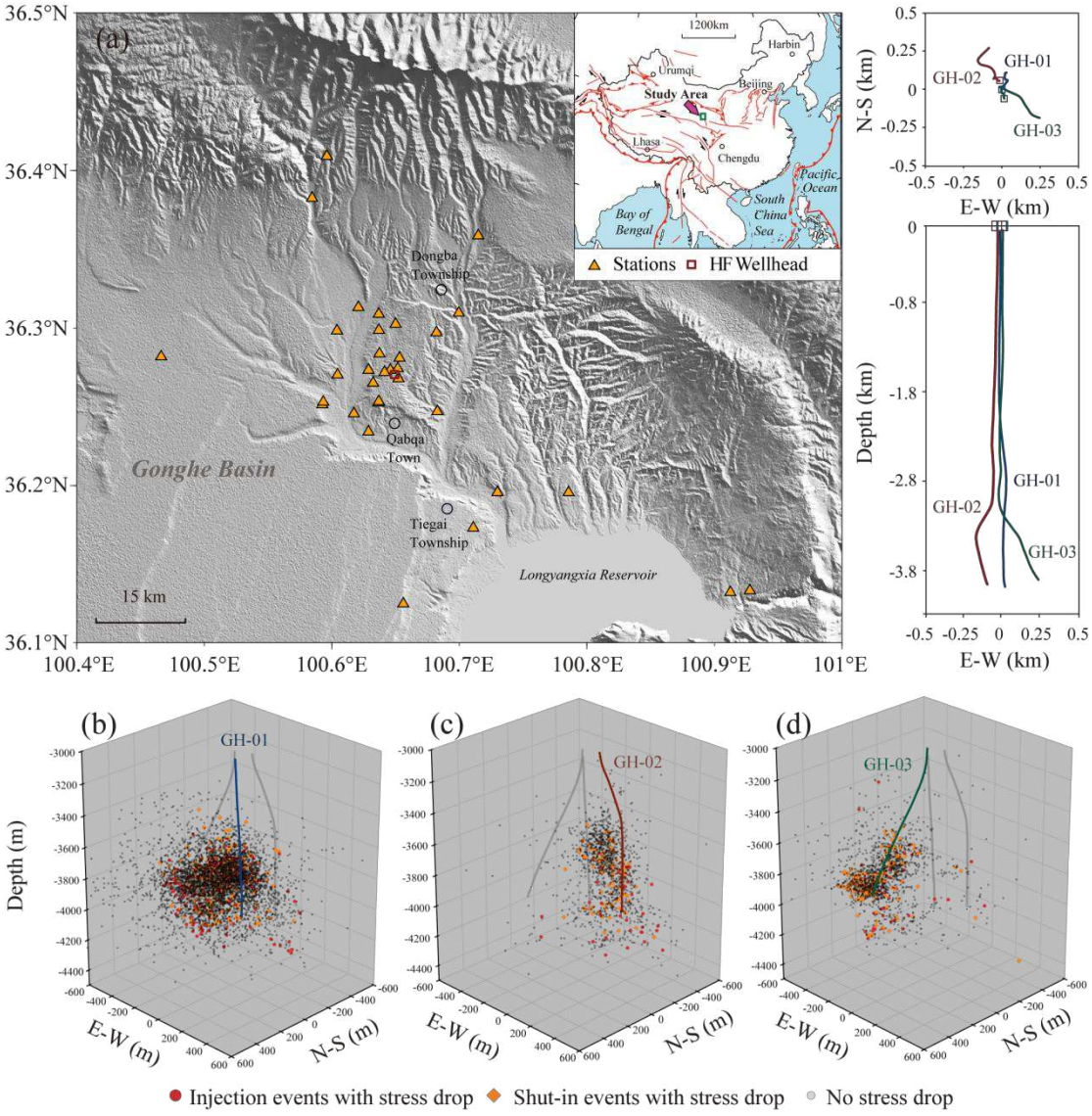



**Figure 1. Map of the study area, seismic network, and spatial distribution of earthquakes**. (a) Shows the distribution of seismic stations and well locations in the study area. The main map marks the wellheads of the three injection wells (GH-01, GH-02, GH-03) and the distribution of seismic stations; the inset in the upper right shows the location of the Gonghe site within China; the right panel shows the surface projection of well trajectories and the East-West depth profile. (b~d) Three-dimensional spatial distribution of earthquakes around wells GH-01, GH-02, and GH-03, respectively (depth range 3000~4500 m). In the figures, red dots represent events with stress drop results during the hydraulic fracturing period, orange diamonds represent events with stress drop results during the shut-in period, and gray dots represent events without stress drop results. The trajectory of the corresponding well is displayed in color, while the trajectories of the other two wells are shown in gray.

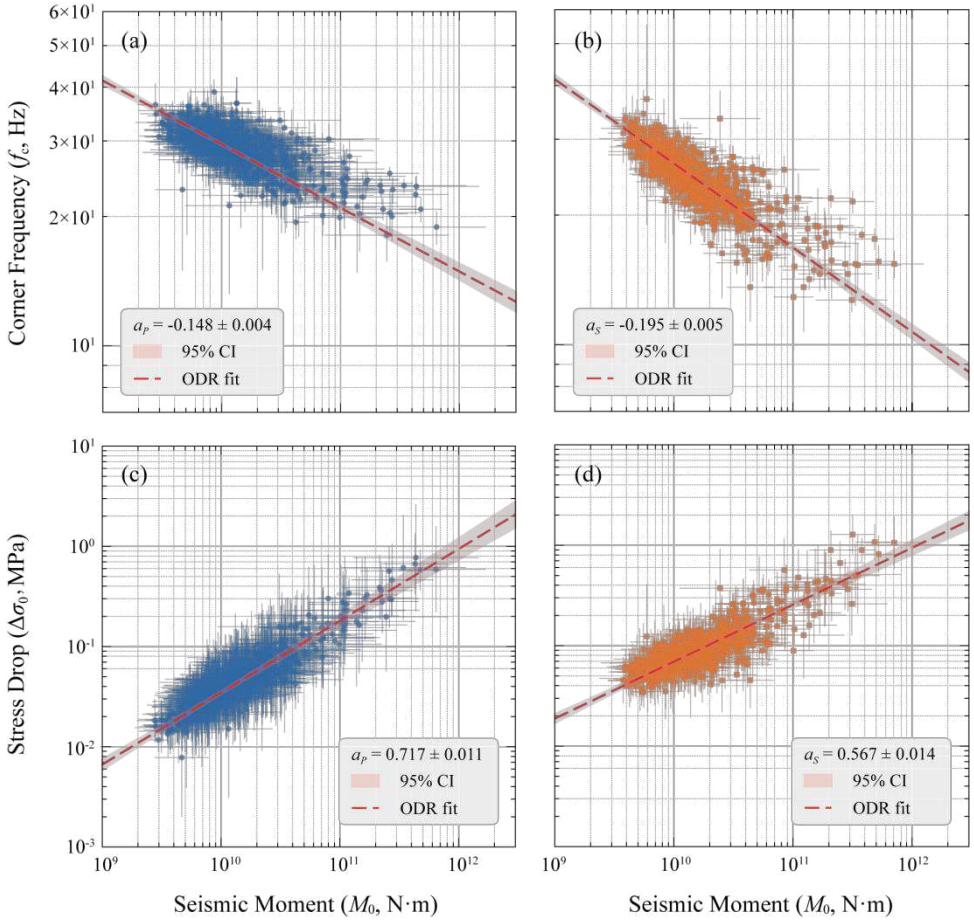



**Figure 2. Scaling relationships of corner frequency ($f_c$) and stress drop ($\Delta\sigma_0$) with seismic moment ($M_0$).** (a) and (b) show the scaling between corner frequency ($f_c$) and seismic moment ($M_0$) derived from P-wave and S-wave data, respectively. (c) and (d) show the scaling between stress drop ($\Delta\sigma_0$) and seismic moment ($M_0$) derived from P-wave and S-wave data, respectively. Error bars are shown for each measurement. The solid red line represents the Orthogonal Distance Regression (ODR) fit, and the shaded pink area indicates the 95% confidence interval.

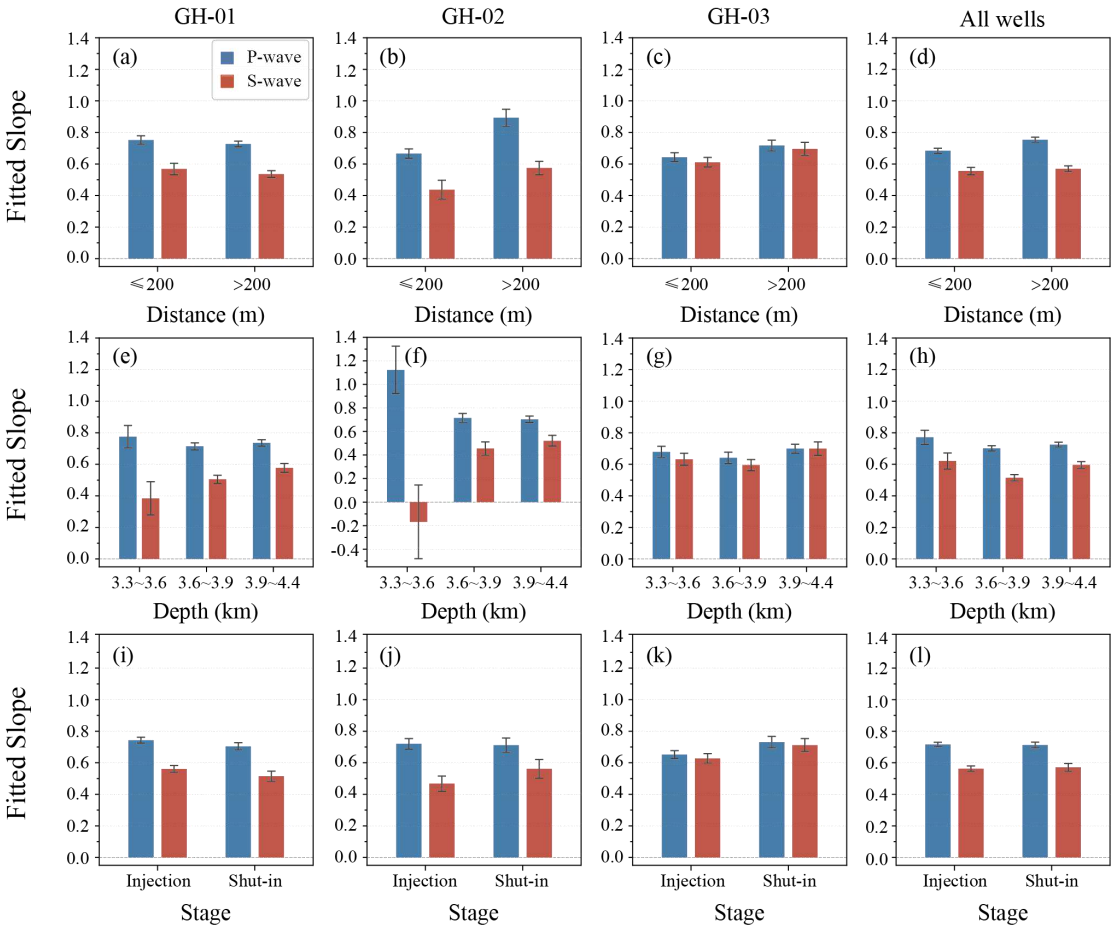



**Figure 3. Comprehensive comparison of stress drop scaling exponents across different geological backgrounds and multi-dimensional conditions**. The first three columns correspond to the GH-01, GH-02, and GH-03 well areas, respectively, while the fourth column represents the combined dataset. Rows represent different grouping conditions: (a~d) comparison between near-well (≤ 200 m) and far-field (> 200 m) zones; (e~h) comparison across depth intervals (overlying layer, stimulation interval, and underlying layer); (i~l) comparison between injection and shut-in phases. In all subplots, blue and red bars represent the scaling exponents for P-waves and S-waves, respectively, with error bars indicating the standard deviation of the fit.

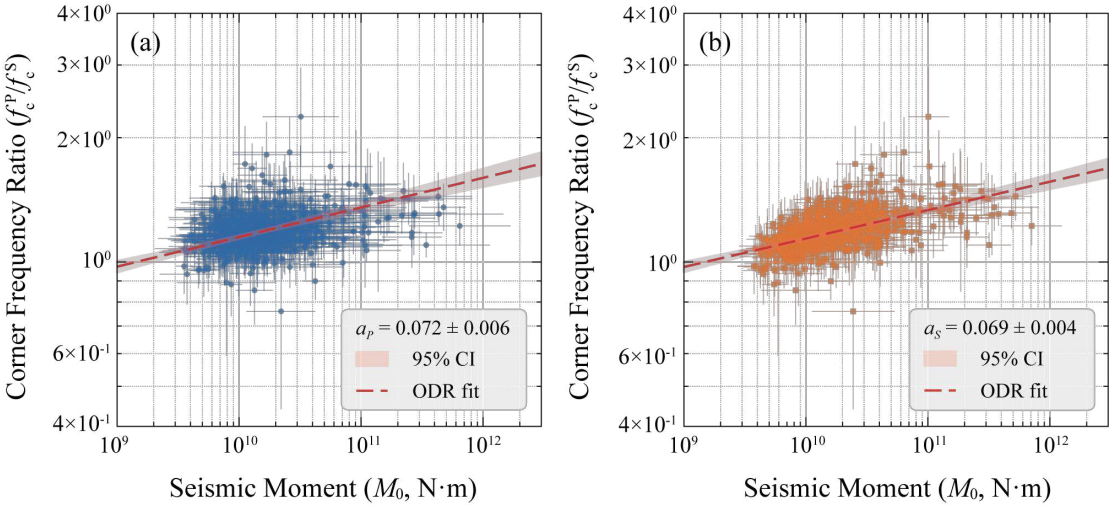



**Figure 4. Variation of P-to-S corner frequency ratio ($f_c^P/f_c^S$) with seismic moment**. (a) and (b) show the ratio plotted against seismic moment estimated from P-wave and S-wave spectra, respectively. Error bars, the Orthogonal Distance Regression (ODR) fit line (solid red line), and the 95% confidence interval (shaded pink area) are shown.

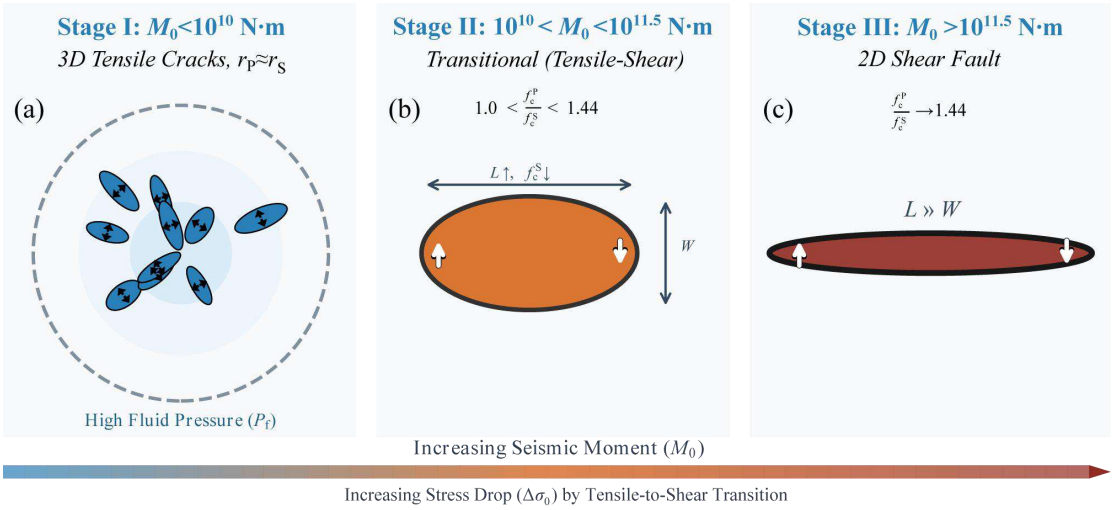



**Figure 5. Conceptual model of rupture geometry and mechanism evolution with increasing scalar seismic moment ($M_0$).** Based on the observed trend of the corner frequency ratio ($f_c^P / f_c^S$), the rupture process is divided into three physical domains. The y-axis represents stress drop, and the x-axis is scalar seismic moment $M_0$. (a) Tensile-dominant domain ($M_0$<$10^{10}$ N·m): Characterized by fluid-driven disordered micro-cracks. Ruptures are approximately isotropic ($L \approx W$), with $f_c^P / f_c^S$ ratios approaching 1.0 and low stress drops. (b) Transitional domain ($10^{10}$< $M_0$ <$10^{11.5}$ N·m): A hybrid tensile-shear mode. As rupture expands, shear components increase, and geometry evolves to be elliptical (length $L$ grows faster than width $W$). The $f_c^P / f_c^S$ ratio falls between 1.0 and the theoretical shear value, causing P-wave stress drop to increase faster than S-wave stress drop. (c) Shear-dominant domain ($M_0$>$10^{11.5}$ N·m): A mature 2D shear fault. The rupture forms a typical shear dislocation model with $L \gg W$. The $f_c^P / f_c^S$ ratio approaches the theoretical shear value (~1.44), and stress drop stabilizes at a higher level. The blue arrow indicates the overall increasing trend of stress drop driven by mechanism transition and geometric evolution.